ACS APPLIED MATERIALS & INTERFACES

www.acsami.org

Research Article

Does Sb_2Se_3 Admit Nonstoichiometric Conditions? How Modifying the Overall Se Content Affects the Structural, Optical, and Optoelectronic Properties of Sb_2Se_3 Thin Films

Ivan Caño,* Pedro Vidal-Fuentes, Lorenzo Calvo-Barrio, Xavier Alcobé, José Miguel Asensi, Sergio Giraldo, Yudania Sánchez, Zacharie Jehl, Marcel Placidi, Joaquim Puigdollers, Victor Izquierdo-Roca, and Edgardo Saucedo

Cite This: *ACS Appl. Mater. Interfaces* 2022, 14, 11222−11234

Read Online

ACCESS | Metrics & More | Article Recommendations | Supporting Information

ABSTRACT: Sb_2Se_3 is a quasi-one-dimensional (1D) semiconductor, which has shown great promise in photovoltaics. However, its performance is currently limited by a high V_{oc} deficit. Therefore, it is necessary to explore new strategies to minimize the formation of intrinsic defects and thus unlock the absorber's whole potential. It has been reported that tuning the Se/Sb relative content could enable a selective control of the defects. Furthermore, recent experimental evidence has shown that moderate Se excess enhances the photovoltaic performance; however, it is not yet clear whether this excess has been incorporated into the structure. In this work, a series of Sb_2Se_3 thin films have been prepared imposing different nominal compositions (from Sb-rich to Se-rich) and then have been thoroughly characterized using compositional, structural, and optical analysis techniques. Hence, it is shown that Sb_2Se_3 does not allow an extended range of nonstoichiometric conditions. Instead, any Sb or Se excesses are compensated in the form of secondary phases. Also, a correlation has been found between operating under Se-rich conditions and an improvement in the crystalline orientation, which is likely related to the formation of a $MoSe_2$ phase in the back interface. Finally, this study shows new utilities of Raman, X-ray diffraction, and photothermal deflection spectroscopy combination techniques to examine the structural properties of Sb_2Se_3, especially how well-oriented the material is.

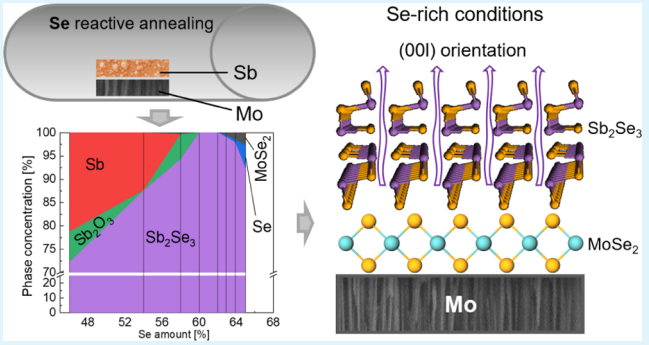

KEYWORDS: *quasi-1D semiconductors, chalcogenides, photovoltaics, Sb_2Se_3, $MoSe_2$, material characterization, emerging materials*

INTRODUCTION

In recent years, thin-film chalcogenide-based photovoltaic (PV) technologies have emerged as one of the most attractive complementary pathways to silicon-based solar cells, opening the door to greater versatility and implementation opportunities for photovoltaics, including flexible and semitransparent devices. Among these innovative absorbers, CdTe and $Cu(In,Ga)(S,Se)_2$ (CIGS) have accomplished remarkable improvements in their power conversion efficiency (PCE), exceeding the 20% barrier.[1,2] Nevertheless, the potentially unstable supply of scarce elements such as In, Ga, and Te and the toxicity of Cd raise doubts about the ability of CIGS and CdTe to meet the necessary industrial demands to transition toward a 100% renewable energy system.[3−5] Consequently, thin-film chalcogenide-based photovoltaics free of critical raw materials remain a highly active research field, generating relevant scientific and technological awareness. For instance, $Cu_2SnZn(S,Se)_4$ (CZTSSe) has aroused great interest as a successful sustainable alternative to CIGS, achieving PCE values of up to 12.6%.[6] However, its chemical complexity makes it difficult to overcome the current limitations, mostly regarding the high number of native defects and secondary phases.[7−9]

In contrast, antimony selenide (Sb_2Se_3) is constituted by earth-abundant and low-toxicity components and possesses a number of highly appealing properties for photovoltaic implementation, such as binary stoichiometry, an optimal band gap (1.2−1.3 eV), a large absorption coefficient, and a quasi-one-dimensional (Q-1D) crystal structure.[10] In addition, solar cells made with this compound can be fabricated in both substrate and superstrate configurations[11,12] at comparatively

Received: October 27, 2021
Accepted: January 14, 2022
Published: March 1, 2022

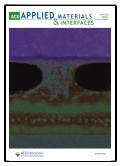

low temperatures,[13] thus paving the way for alternative substrates and architectures. Furthermore, Sb_2Se_3 has shown great promise not only for photovoltaics but also for energy storage, achieving a high reversible capacity of 312.03 mAh/g at a current density of 1000 mA/g for potassium-ion batteries (PIBs).[14,15] The Q-1D structure of Sb_2Se_3 consists of $(Sb_4Se_6)_n$ covalently bonded ribbons along one crystallographic direction, while they are stacked by weak van der Waals forces in the other two directions,[16] conferring strong anisotropic optoelectronic properties, such as preferential carrier transport in the [001] direction (along the covalently bonded ribbons according to *Pbnm* #62). Hence, by tuning the crystalline orientation of the Sb_2Se_3 film, it is possible to increase the minority carrier mobility and collection and thus improve the photovoltaic (PV) performance of the device.[17] Thus far, it has been reported that the substrate on which the Sb_2Se_3 is grown has a significant influence on the ribbon alignment, along with the temperature at which the material is subjected during synthesis (with a reported optimal T range of 300−330 °C).[18−20] However, the effect of the relative amount of Se/Sb on the film's crystalline orientation is yet to be thoroughly investigated.

In a very short time, Sb_2Se_3 has shown steady improvements in the PV performance, achieving record cell efficiencies of 9.2% (nanorod arrays) and 8.5% (planar heterojunction solar cells), prepared by close-spaced sublimation,[11,21] and 6.84% by magnetron sputtering.[22,23] However, devices are still mainly limited by a high V_{oc} deficit, suggesting that recombination processes involving deep defects might be a limiting factor.[24,25] Indeed, despite being a relatively simple binary compound, it has been shown by first-principles calculations that the intrinsic defects in Sb_2Se_3 are unexpectedly complicated and unconventional, with up to three different V_{Se} and two V_{Sb} components due to several nonequivalent atomic sites, in addition to substitutional and intrinsic defects and other uncommon defects, such as 2Se replacing one Sb antisite ($2Se_{Sb}$).[26] There is consequently a clear interest in exploring novel strategies that make it possible to control the emergence of these defects and to offer new conditions to unlock the whole potential of the absorber.

In particular, modulating the relative amount of Se/Sb by moving away from the stoichiometric conditions could offer an opportunity to compensate defects, while modifying the electronic properties of the material, without adding new components (i.e., complexity) to the system. For instance, according to Huang et al.,[26] the electrical conductivity could be tuned from p-type to n-type by modulating the Se chemical potential through transitioning from Se-rich to Se-poor conditions. Moreover, it has been reported by theoretical studies that deep defects have a higher concentration under Sb-rich conditions, suggesting that a hypothetical strategy to enhance the performance of the device could be by favoring a Se-rich synthesis.[24] However, it is still unclear whether Sb_2Se_3 allows an extended off-stoichiometric range or, on the contrary, grows forming a single phase highly resilient to compositional variations. Indeed, off-stoichiometric film composition has been a key element in the past success of mature thin-film chalcogenide absorbers such as CIGS or CZTSSe, especially in terms of control of the minority carrier concentration.[27−29] For example, it has been shown that the shallow defect V_{Cu} in kesterites becomes dominant under Cu-poor conditions, contributing to an enhanced p-type conductivity.[30,31]

Considering these relevant characteristics of chalcogenide absorbers such as CIGS and CZTSSe, it is extremely important to investigate the tolerance of Sb_2Se_3 to intrinsic doping and compositional variations, moving toward a broader understanding of this material with the goal of developing improvement strategies based on verifiable empirical knowledge.

Remarkably, recent experimental evidence has revealed that moderate Se excess increases the PV performance of Sb_2Se_3/CdS p-n junction-based devices.[32,33] Nonetheless, whether this excess has been incorporated into the structure or segregated in the form of additional phases is still unclear.

Here, we have used a sequential process based on the selenylation of thermally evaporated Sb to synthesize a series of Sb_2Se_3 thin films with different Se/Sb relative contents, ranging in a wide spectrum of nominal compositions. By forcing the incorporation of different Se amounts, we expected to elucidate whether the Se and Sb excesses had been incorporated into the Sb_2Se_3 structure and thus determine whether Sb_2Se_3 is a highly stoichiometric single-phase semiconductor in the same manner as in CdTe or it admits an extended compositional range as it occurs in CIGS or CZTS. Also, we have identified all the phases that appear under the different conditions studied, with which we have been able to develop a phase diagram as a function of the overall Se content. Interestingly, we have detected a correlation between the amount of the self-generated $MoSe_2$ phase and the preferential crystalline orientation of Sb_2Se_3, proving that the presence of such a phase is critical to obtain good-quality devices with an optimal orientation. Finally, prototype solar cells have been fabricated and characterized to assess the effect of varying the Se content in the absorber on the PV performance of the device.

EXPERIMENTAL METHODOLOGY

Material and Device Preparation. Sb_2Se_3 layers were manufactured on Mo-sputtered SLG substrates (SLG/Mo), using a two-step sequential process consisting of the deposition of a 250 nm Sb layer followed by reactive annealing under a Se atmosphere. Sb coating was performed by thermal evaporation (Oerlikon Univex 250), from Sb shots (Alfa Aesar, 1−3 mm), using a base vacuum of 10^{-5} mbar and an evaporation rate of 1 Å/s. Then, the SLG/Mo/Sb precursors were subjected to Se reactive annealing in a tubular furnace, using a semiclosed graphite box (23 cm^3). Accordingly, samples were heated up to 320 °C (with a 20 °C/min heating ramp) at 500 mbar and then cooled naturally (45 min approximately). To explore different compositions, different annealing durations were applied between 15 min (Se-poor) and 30 min (Se-rich). Likewise, the Se availability was modulated by changing the amount of Se powder placed in the graphite boxes, without any condition below the threshold required to achieve a saturated atmosphere. To synthesize Sb-rich films (Se contents below its stoichiometric amount), 10−15 mg of Se powders was used (Alfa Aesar, Se powder 200 mesh). On the other hand, to synthesize Se-rich samples, approximately 25 mg was placed in the boxes. The appropriate contents in each case were determined through previous optimization processes. Importantly, graphite boxes are subjected to high-temperature cleaning (650 °C, 2 h) beforehand to eliminate any possible selenium excess in between each sample processing.

To characterize the optoelectronic properties, some of the Sb_2Se_3 layers prepared in accordance with the previous procedure were converted into solar cells. The heterojunction was completed with an n-type CdS buffer deposited by chemical bath deposition, followed by i-ZnO + indium tin oxide (ITO) deposition by direct current (DC) pulsed magnetron sputtering (Alliance Concept CT100), as reported elsewhere.[34]

https://doi.org/10.1021/acsami.1c20764
ACS Appl. Mater. Interfaces 2022, 14, 11222−11234

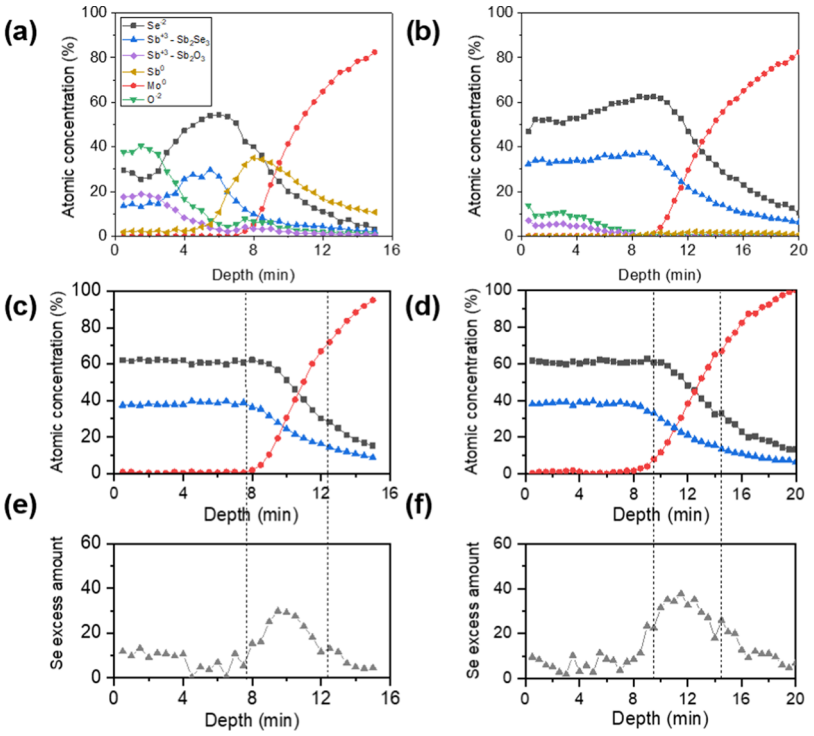

Figure 1. XPS in-depth profiles of samples with a nominal composition of 2[Se]/(2[Se] + 3[Sb]): (a) 0.36, (b) 0.48, (c) 0.53, and (d) 0.54, (e, f) distribution of Se out of the stoichiometry for the 0.53 and 0.54 samples, respectively.

Material and Device Characterization. The nominal composition and thickness of the as-synthesized Sb_2Se_3 absorbers were determined by X-ray fluorescence (XRF) with Fischerscope XVD equipment, which was previously calibrated by inductively coupled plasma mass spectrometry (ICP-MS). Cross-sectional morphology and thickness of complete devices were characterized by scanning electron microscopy (SEM), using a Zeiss Series Auriga field-emission microscope, with an acceleration voltage of 5 kV and working distances ranging between 3 and 5 mm. Composition profiles were studied by X-ray photoelectron spectroscopy (XPS) in the CCiTUB with a PHI 5500 multitechnique system from Physical Electronics, using a monochromatic X-ray source Al Kα line of 1486.6 eV. X-ray diffraction (XRD) data were obtained using a PANalytical X'Pert PRO MPD alpha1 Bragg-Brentano powder diffractometer, with a Cu tube operating at 45 kV and 40 mA, a Johansson-type Ge (111) primary focalizing monochromator, and a solid-state strip 1D PIXcel^{1D} detector. High-resolution, high-statistics, full-angular range Cu Kα_1 $\theta/2\theta$ scans were performed with the following parameters: $2\theta/\theta$ scans from 4 to 145°; step size of 0.0131°; measuring time per step of 200 s (PIXcel^{1D} active length of 3.347°); three consecutive repeated scans; total measuring time per sample of 7.2 h. An automatic divergence slit system and a mask enabled a constantly irradiated surface (10 × 12 mm^2) over the analyzed samples. The diffracting volume is also constant regarding the small and finite thickness (below 2 micrometers) of the characterized layers. Full profile analysis has been performed, applying Rietveld refinement for all the crystalline structure phases observed.[35] The refinements have been performed with TOPAS v6 software.[36] The peak width of each phase was modeled with the double-Voigt approach by considering both the Lorentzian contribution of the crystallite size effect and the Gaussian contribution of the microstrain to the peak width.[37] Preferential orientation corrections were applied by spherical harmonics or alternatively by the March–Dollase function.[38] The background was modeled with a 15th-order Chebyshev polynomial. The instrumental contribution to the diffraction profile was calculated with the fundamental parameters approach.[39] Raman spectroscopy measurements were performed with an optical probe in the backscattering configuration developed at IREC facilities coupled to a FHR640 Horiba Jobin Yvon spectrometer, where the signal is acquired with a liquid nitrogen-cooled (140 K) CCD detector. The excitation wavelength employed was 633 nm and was focused on a macrospot (~50 μm) to avoid sample inhomogeneity. The laser power was kept under 25 mW/cm^2 to avoid degradation of the films.

Additionally, the optical absorption of glass (Corning1737)/Sb_2Se_3 samples was characterized by photothermal deflection spectroscopy (PDS). This technique was used to determine the absorptance of the Sb_2Se_3 films in the sub-band gap region. A single-slab model was applied to compute the absorption coefficient (see the Supporting Information for a more detailed description of the procedure). The transverse PDS setup used in this work consists of a 100 W tungsten halogen lamp, PTI 01-0002 monochromator (two-grating monochromator, spectral range of 400–2000 nm), and Thorlabs MC1000 optical chopper (4 Hz light modulation frequency). A Signal Recovery 7265 lock-in amplifier was connected to a Hamamatsu C10442-02 PSD position-sensitive detector to measure the deflection of a MC6320C 10 mW laser probe beam. Samples were put in a quartz cell filled with Fluorinert TM FC-40. A personal computer was used to control the monochromator, change the order filters, and store the PDS signal read from the lock-in amplifier.[40]

SLG/Mo/Sb_2Se_3/CdS/ZnO/ITO devices were characterized by current density–voltage measurements ($J-V$ curves), using a Sun 3000 AAA-class Abet solar simulator, with a uniform illumination area of 15 × 15 cm^2, calibrated with a Si reference solar cell. Optoelectronic characterization was performed on individual 3 × 3 mm^2 cells, insulated by mechanical scribing (Micro Diamond MR200 OEG), without a contact grid or antireflective coating.

RESULTS

Compositional and Structural Analysis of Sb_2Se_3 Nonstoichiometric Thin Films. SLG/Mo/Sb_2Se_3 thin films were prepared following the aforementioned experimental methodology. The XRF analysis of the samples revealed that the suggested two-step process allowed us to obtain Sb_2Se_3 thin films with the Se amount ranging from 0.36 to 0.55 (2[Se]/(2[Se] + 3[Sb])), where 0.50 corresponds to the

https://doi.org/10.1021/acsami.1c20764
ACS Appl. Mater. Interfaces 2022, 14, 11222–11234

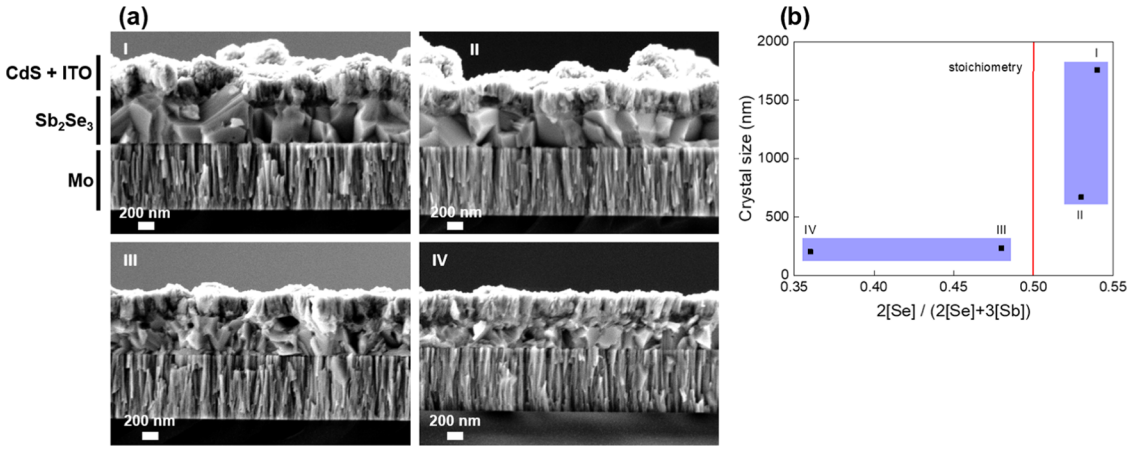

Figure 2. (a) SEM cross-sectional 30× images of samples with 2[Se]/(2[Se] + 3[Sb]): (I) 0.54, (II) 0.53, (III) 0.48, and (IV) 0.36. (b) Crystalline domain as a function of 2[Se]/(2[Se] + 3[Sb]), obtained from the XRD−Rietveld analysis.

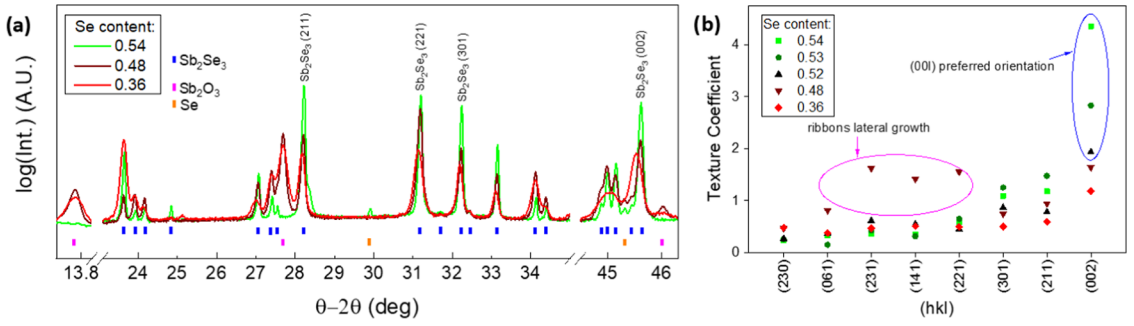

Figure 3. (a) X-ray diffractograms of a set of samples with different 2[Se]/(2[Se] + 3[Sb]) relative amounts. ICDD Powder Diffraction File pattern numbers are Sb_2O_3: 01-072-1334 and Sb_2Se_3: 04-003-0715. (b) Texture coefficients of diffraction peaks of Sb_2Se_3 thin films with different Se amounts.

stoichiometric conditions. Thus, it was proved that sequential thermal evaporation and reactive annealing synthesis, with control over Se vapor pressure and annealing time, allowed us to incorporate different amounts of Se into the thin films. However, XRF indicated the elemental content in the sample, regardless of whether it forms a single phase or several secondary phases.

To determine the elemental distribution of the films and to elucidate whether the material admits an extended non-stoichiometric range, in-depth XPS analysis was performed for the different compositions, as shown in Figure 1. In all the cases, it is observed that after a certain sputtering time, the Mo signal increases abruptly, denoting the back Mo/Sb_2Se_3 interface. Also, atomic concentrations of Se^{-2} (black spots) and Sb^{+3}—in Sb_2Se_3—(blue spots) evolve correlatively, indicating that the Sb_2Se_3 composition remains steady throughout the film thickness, regardless of the overall Se content as measured by XRF. This suggests that Sb_2Se_3 is a single-phase stoichiometric material, whereby any Se or Sb excess in the sample is compensated as secondary phases, rather than forming off-stoichiometry Sb_2Se_3. Indeed, for Sb-rich conditions (see Figure 1a,b), an Sb_2O_3 phase has been detected at the front of the cell, the amount of which increases as the nominal Se content decreases, indicating that unreacted Sb on the surface of the film has been oxidized following the annealing process, once the material came in contact with air. Interestingly, it is observed that Se has a lower concentration near the surface than in the deeper region of Sb-rich samples (0.36 and 0.48, respectively). A possible hypothesis would be that during the heating ramp, there exists a Se flux toward Mo, before the Sb_2Se_3 crystallizes upon reaching its formation temperature around 320 °C. Under Se-deficit conditions, most Se element will have diffused to the back, leading to the aforementioned Sb_2Se_3 profile. Recent experiments with interrupted growth processing have shown similar trends; however, more experiments are required to unequivocally confirm the hypothesis.[41] Finally, Figure 1a shows a high amount of metallic Sb at the back of the absorber, suggesting that the very low Se amount in such a sample is insufficient to react with the Sb precursor throughout its entire thickness.

On the other hand, in the samples with 0.53 and 0.54 Se amounts (see Figure 1c,d), an offset between the Se^{-2} and Sb^{+3} signals, overlapping the Mo curve, is observed. This may indicate that a Se-rich phase has appeared in the back contact interface. To observe more clearly the distribution of Se under these circumstances, the amount of Se in excess (beyond stoichiometry) has been plotted as a function of the sputtering time; see Figure 1e,f. Interestingly, it can be noticed that the Se excess remains fairly low for most of the layer (within the noise range), while significantly increasing in the rear interface. The fact that the amount of Se excess at the back interface increases as the film becomes Se-richer supports the hypothesis that under Se-excess conditions, a Mo−Se phase appears, whose content increases as the overall Se content increases. This phase is likely to be $MoSe_2$, as consistently reported for chalcogenide films grown on the Mo substrate.[42−44]

To study the structural properties of the Sb_2Se_3 phase in either of the previous cases, SEM cross-sectional images of the

https://doi.org/10.1021/acsami.1c20764
ACS Appl. Mater. Interfaces 2022, 14, 11222−11234

completed devices are acquired; see Figure 2a. Images have been obtained from complete devices (including buffer and window layers)—see Figure S1 for a complete energy dispersive X-ray analysis (EDX) profile and mapping compositional analysis of the layers constituting a sample. Interestingly, the Se-rich films (I and II) have large grains all developed alongside the entire thickness of the layer, while the Sb-rich samples (III and IV) exhibit smaller grains scattered throughout the thickness of the layer (see Figure S2 for lower magnification images). Moreover, the shape of the grains appears much more random in these samples, whereas I and II show well-oriented grains in the growth direction. To delve deeper into the crystalline orientation and structure of nonstoichiometric Sb_2Se_3, a detailed XRD full-profile Rietveld analysis was performed; see Table S1. The average crystal size (Lorentzian) shows a clear threshold around stoichiometric conditions (0.50), from which the crystal size increases significantly as the overall Se amount increases, whereas by shifting toward Sb-rich conditions, it drops abruptly and the slope becomes much less pronounced; see Figure 2b. Importantly, this diverging behavior between Se-rich and Sb-rich conditions clearly implies a change in the growing conditions that favors a more orderly and controlled formation of the grains; one of the goals of this work is to determine the cause. As shown below, this trend is consistently repeated with the other material properties under analysis.

Figure 3a shows the X-ray diffractograms of samples in each of the compositional ranges of interest for this study, i.e., Sb-rich (2[Se]/(2[Se] + 3[Sb]) = 0.36), slightly Sb-rich/near stoichiometry (0.48), and moderately Se-rich (>0.54), focusing on the selected 2θ ranges; see Figure S3 for the complete 10−140° diffractograms, the Rietveld-calculated patterns, and the difference between the experimental and theoretical patterns. Since the XRD analysis was performed on Mo/Sb_2Se_3 samples, the main crystalline phases include Mo (back contact layer) and Sb_2Se_3 (absorber). Also, for the Se-rich films, a certain amount of $MoSe_2$ and Se secondary phases have been detected, which increase as the overall concentration becomes Se-richer (see Table S1 for main Rietveld refinement analysis parameters including the phase amount, crystal size, and cell volume). In contrast, for Sb-rich thin films, these phases are not observed; however, important amounts of α-Sb_2O_3 (0.48, 0.36) and m-Sb (0.36) are detected, whose content also increases as the composition becomes Se-poorer. The presence of the Se and α-Sb_2O_3 phases in each group of the samples is directly corroborated from the diffractograms; see Figure 3a. Although with very weak and wide peaks, which are difficult to identify, reflections corresponding to $MoSe_2$, mainly oriented in the (001) direction, have been detected and quantified in the Se-rich samples by Rietveld analysis (Table S1); see Figure S4 for the enlarged diffractogram in the 11−15° region, where the $MoSe_2$ peak (003) appears.[45,46] Moreover, a change in the Sb_2Se_3 crystallinity depending on the Se content in the films can also be observed. Overall, Sb_2Se_3 layers show a complex multiaxial crystallinity, with a [001]-preferred orientation (also in the [hk1] and [h01] directions), which is manifested by the intense and sharp peaks observed at 45.6° (002), 29.2° (211), 31.2° (221), and 32.2° (301). Interestingly, as the Se content decreases, these reflections become broader and their intensity declines, until no preferential texture is visibly discerned for the sample with the lowest Se amount. Therefore, it is shown that despite a single-phase stoichiometric material, the crystalline orientation and structure of Sb_2Se_3 are indeed affected by the overall Se content of the film, exhibiting a good [001]-preferred orientation for Se-rich samples and deteriorated randomized texture in the Sb-rich range. To quantitatively assess the differences in the crystalline orientation between samples with a distinct Se concentration, the texture coefficient (TC) of the selected Bragg reflections was calculated based on eq 1, where N is the number of reflections considered for the calculation, I_{hkl} is the measured empirical intensity of a diffraction peak, and $I_{0,hkl}$ corresponds to the intensity value in the standard XRD pattern (ICDD 04-003-0715 Powder Diffraction File patterns).[47,48]

$$\mathrm{TC}_{hkl} = \frac{I_{hkl}/I_{0,hkl}}{\frac{1}{N}\cdot\sum_{i=1}^{N} I_{h_ik_il_i}/I_{0,h_ik_il_i}} \quad (1)$$

The results of the TC calculations from a series of selected Sb_2Se_3 samples are illustrated in Figure 3b. Notably, samples with Se excess and most specially those with 0.54 Se are primarily dominated by the (002) reflection. Since the h and k Miller indices are both 0, this indicates that $(Sb_4Se_6)_n$ ribbons grow perpendicularly to the substrate surface, proving that Se-rich conditions help enhance the orientation of Sb_2Se_3 grains. On the other hand, as we shift toward Sb-rich conditions, the (231), (141), and (221) peaks become dominant. In this case, h and k values are greater or equal to 3, indicating that the angles between the $(Sb_4Se_6)_n$ ribbons and substrate are small, revealing an Sb_2Se_3 lateral growth deemed detrimental to the electrical properties of the material.[17] Finally, we observe that the sample with 0.36 Se has a virtually arbitrary crystalline orientation, with all TC presenting very small, similar values between 0 and 1. However, we note that this sample has the smallest value of TC_{002} and the largest value of TC_{230}, indicating a total loss of the preferred orientation in the (002) direction.

In addition, the XRD−Rietveld analysis has showed a connection between the cell volume and the overall Se amount; see Figure S5. First, it is noticed that the cell volume of Sb_2Se_3 thin films is smaller than that of the bulk monocrystals.[49] This reduction of the volume could be associated with a decrease of Se_{Sb} and $2Se_{Sb}$ defects and an increase of V_{Se} vacancies, allegedly reducing the Fermi level splitting (which could affect negatively the V_{oc} since Se_{Sb} is responsible for p-type conductivity).[26] Interestingly, near stoichiometry, this compressive effect is larger, with samples having a cell volume of 543.3 Å^3 against that of 545.6 Å^3 of a single crystal, while for the Se(Sb)-richer films, a sequential increase is observed as the nominal composition moves away from stoichiometry, the cell volume becoming more similar to that of the single crystal. It is possible that an increase in the overall Se content compensates the detrimental V_{Se} defects, lessening the compressive strain, hence the volume enlargement. However, further research is required to assess the effect of changing the Se amount on the defect structure of Sb_2Se_3, in particular at the intrinsic doping level (since otherwise it has been proven that Sb_2Se_3 does not admit off-stoichiometry compositions) and how this can affect the cell volume.

Complementing the previous study of structural properties by XRD and now paying special attention to the characterization of interfaces (both the surface and back interface), a complete Raman spectroscopy analysis was performed. The average Raman spectra of bare Sb_2Se_3 thin films (surface) with a nominal composition in the range of 0.36 < 2[Se]/(2[Se] + 3[Sb]) < 0.54 are shown in Figure 4a. The formation of the α-

https://doi.org/10.1021/acsami.1c20764
ACS Appl. Mater. Interfaces 2022, 14, 11222−11234

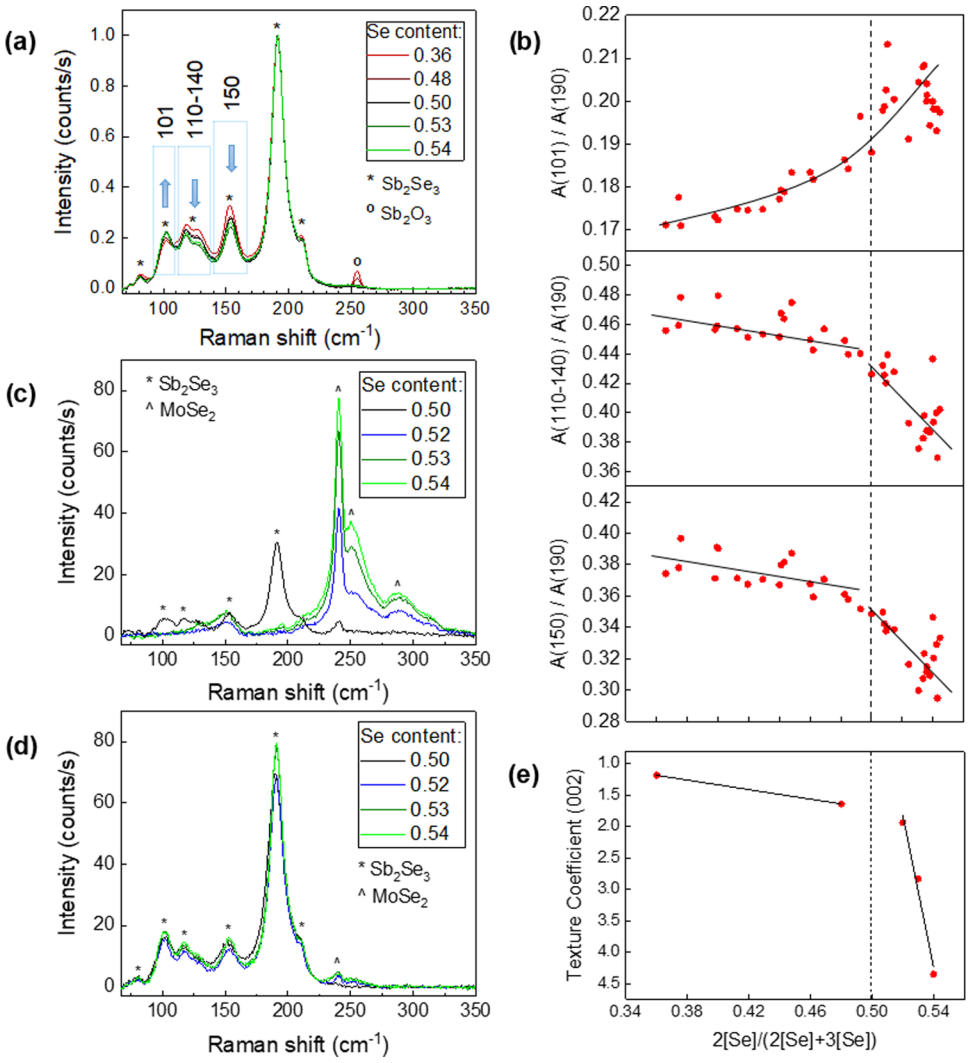

Figure 4. (a) Normalized Raman spectra of the surface of Sb_2Se_3 thin films with 2[Se]/(2[Se] + 3[Sb]): 0.36, 0.48, 0.50, 0.53, and 0.54. (b) Area of Raman peaks—expressed as A(peak of interest)/A(190 cm^{-1}) as a function of 2[Se]/(2[Se] + 3[Sb]). (c) Absolute Raman spectra of lift-off remain on the Mo substrate of Sb_2Se_3 samples with 2[Se]/(2[Se] + 3[Sb]): 0.50, 0.52, 0.53, and 0.54. (d) Absolute Raman spectra of the previous peeled-off Sb_2Se_3 films. (e) Texture coefficient (002) as a function of 2[Se]/(2[Se] + 3[Sb]).

Sb_2O_3 secondary phase, which appears only on the surface of Sb-rich samples (peak at 254 cm^{-1}), is also detected.[49−51] On the other hand, elemental Se phases (t-Se)[49,52] have been detected in the Se-richer samples; see Figure S6. Furthermore, the following trends in some areas of the Raman peaks associated with the Sb_2Se_3 phase are also observed (boxed areas in Figure 4a):

1. The area of the Sb_2Se_3 peak at 101 cm^{-1} increases as the overall Se amount increases.
2. The area of the Sb_2Se_3 peaks between 110 and 140 cm^{-1} decreases as the overall Se amount increases.
3. The area of the Sb_2Se_3 peak at 150 cm^{-1} decreases as the overall Se amount increases.

As previously reported by Fleck et al.,[53] an enhanced ribbon alignment in the [001] direction leads to minimization of the Raman signal at 150 cm^{-1}, proving that Raman spectroscopy allows us to quickly and easily assess the quality of the crystalline orientation in Sb_2Se_3 thin films. In addition, it is shown here that the areas defined by the 101 and 110−140 cm^{-1} peaks also experience clear variations depending on the 2[Se]/(2[Se] + 3[Sb]) relative concentration of the films increasing and decreasing. The fact that these variations occur in samples where the Sb_2Se_3 phase is single-phase stoichiometric, as shown with XPS, but with different crystalline orientations (see Figure 3) leads us to think that the area defined by the 101 and 110−140 cm^{-1} signals is also contingent on the loss of the (002)-preferred orientation, which will be discussed later. The probing depth of the Raman measurements is surface-sensitive (~100 nm), although their consistency with other methods (XRD), the small thickness of the films (~800 nm), and the relatively large size of grains (Figure 2) allow us to hypothesize that these observations are also valid throughout the entire film thickness.

Further analysis related to the area variations in Raman spectra and their correlation with the Sb_2Se_3 nominal composition of several samples (including samples with a lateral compositional gradient) has been performed; see Figure 4b. Hence, the areas of the 101, 110−140, and 150 cm^{-1} Raman peaks, normalized to the main Sb_2Se_3 signal at 190 cm^{-1}, have been plotted as a function of 2[Se]/(2[Se] + 3[Sb]). Accordingly, it is clearly noticed that there is a threshold around 0.50 Se, so that for increasing Se amounts,

https://doi.org/10.1021/acsami.1c20764
ACS Appl. Mater. Interfaces 2022, 14, 11222−11234

the areas of signals at 150 and 110−140 cm^{-1} stop decreasing at the same rate, and the slope becomes more pronounced. Significantly, these behaviors present similarities with the trends in the crystal size (Figure 2b) and texture coefficient, TC (Figure 4e), where TC_{002} also shows a continuously decreasing slope that becomes more pronounced as the Se amount increases beyond the stoichiometric point. Thus, it is confirmed that both the 110−140 cm^{-1} band and 150 cm^{-1} peak reflect changes in the crystalline orientation, with their areas decreasing as the (002) direction becomes dominant. Otherwise, the 101 cm^{-1} signal presents a similar behavior with a positive slope, which is consistent with the opposite symmetry of this peak. The trend may not be as clear as that for the 110−140 and 150 cm^{-1} signals; however, the area of integration is also smaller, leading to the signal/noise ratio of the measurement affecting more pronouncedly the dispersion of data points.

These observations raise a question: if Sb_2Se_3 is indeed a stoichiometric material, why does it have an enhanced ribbon alignment when the overall composition is Se-rich? To delve deeper into this behavior, a mechanical lift-off of a series of samples with different 2[Se]/(2[Se] + 3[Sb]) nominal concentrations was performed. See Figure 4c for the lift-off remains on the Mo substrate for samples with the Se concentration ranging from 0.50 to 0.54. Interestingly, a $MoSe_2$ phase has been identified, whose content increases as the overall Se amount also increases, while for the stoichiometric sample (0.50), Sb_2Se_3 is observed and only traces of $MoSe_2$ are detected. Note that this trend coincides with the loss of the (002)-preferred orientation as shown by XRD and Raman. Thus, it is likely that the *in situ* formation of $MoSe_2$ plays a crucial role in the growth of well-oriented Sb_2Se_3. Likewise, the absence of $MoSe_2$ leads to a more randomized grain growth, without the optimal ribbon alignment perpendicular to the substrate, which is likely to negatively affect the device performance due to lower conductivity across the parallel-stacked ribbons. This has been further validated by preparing an SLG/Sb_2Se_3 sample following identical synthesis conditions to those for manufacturing an SLG/Mo/Sb_2Se_3 (0.54 Se) film and performing the corresponding XRD analysis; see the diffractogram in Figure S7 and calculated TCs in Table S2. The TC_{002} of an SLG/Sb_2Se_3 sample (1.8) is significantly lower than that of Se-rich SLG/Mo/Sb_2Se_3 (4.4). Moreover, TC_{230} is larger (0.8 against 0.2 of SLG/Mo/Sb_2Se_3), showing that films directly grown on glass do not present a (002)-preferred crystalline orientation. Finally, additional Raman measurements are performed on the peeled-off Sb_2Se_3 film (see Figure 4d), where the expected Sb_2Se_3 signals can be easily noticed, along with some of $MoSe_2$, whose amount increases as the film becomes Se-richer.

Here, it has been demonstrated that an enhanced Sb_2Se_3 ribbon alignment leads to both a decline in the area of 150 and 110−140 cm^{-1} Raman peaks and an increase of the 101 cm^{-1} signal, deeming Raman spectroscopy as a powerful technique to assess how well-oriented the material is. Additionally, two discrepant trends have been reported based on the Se nominal composition, denoting that variations in the crystalline orientation, as shown in Figure 4b,e, must originate from two combined effects: first, the increasing annealing times between samples 0.36 and 0.50 (15−30 min), leading to a progressive and soft enhancement of the preferred [hk1] orientation until stoichiometry is reached (slope of 0.2 cm^{-1} in Figure 4b, 110−140 and 150 cm^{-1} peaks); and second, the augmenting content of $MoSe_2$ in samples 0.50−0.55, producing an abrupt change of slope (1 cm^{-1} in Figure 4b) and ribbon alignment, leading to fully oriented grains in the (001) direction. These observations confirm previous accounts by Li et al.,[48] where selenylation of Mo prior to the Sb_2Se_3 deposition led to an enhancement of [*kh*1]-oriented grains. The fact that $MoSe_2$ has a preferred crystalline orientation in the (001) direction (see Rietveld analysis in Table S1) suggests that the preferential perpendicular growth of $MoSe_2$ favors the vertical anchoring of $(Sb_4Se_6)_n$ ribbons, forming oriented Sb_2Se_3 grains in the (002) direction.[43,54] Therefore, modifying the texture of the back contact (from Mo to the Mo/$MoSe_2$ system) ultimately affects the formation of Sb_2Se_3 by enhancing its selectively oriented growth in the (001) direction, essential to develop a good quasi-1D structure. This is supported by previous research, according to which the substrate affects all electronic, structural, and crystallographic properties of the absorber.[18,19]

Regarding the role of $MoSe_2$, we can point to two factors that lend weight to our hypothesis about its effect on the oriented growth of Sb_2Se_3. First, since the enthalpy of formation of $MoSe_2$ (− 234.4 kJ/mol) is negative and smaller than that of Sb_2Se_3 (−128.7 kJ/mol), i.e., $MoSe_2$ is thermodynamically favored under our manufacturing conditions; and experimental evidence indicates that there is a Se flux toward Mo during the heating process (see Figure 1), it is plausible to assume that the $MoSe_2$ layer is formed in the first place, effectively influencing the subsequent Sb_2Se_3 crystallization.[55] Second, the lattice mismatch (see eq 2, where ε stands for the mismatch and a_i is the lattice parameter of each layer) of the $MoSe_2/Sb_2Se_3$ interface is significantly smaller (8%) than that of Mo/Sb_2Se_3 (26%) when both the substrate and layer are oriented in the *c* direction; see the lattice constants and mismatch in Table S3.[56−58] This indicates that the strain between $MoSe_2$ and Sb_2Se_3 layers with the preferred crystalline orientation is lower than that of the Mo/Sb_2Se_3 system, which may contribute to a more ordered ribbon growth in the first case. Also, a mismatch larger than 20% inevitably implies the formation of incoherent interfaces, while for ε < 10%, the system may be strained but leads to coherent interfaces.[59]

$$\varepsilon = \frac{a_{Sb_2Se_3} - a_{substrate}}{a_{substrate}} \quad (2)$$

To sum up, the previous compositional and structural analysis of Sb_2Se_3 nonstoichiometric thin films has led to the following observations:

- Sb_2Se_3 is a single-phase compound that does not allow an extended range of nonstoichiometry conditions. Indeed, any Sb or Se excess is compensated in the form of secondary phases: Sb_2O_3 and m-Sb for Sb-rich conditions and $MoSe_2$ and amorphous Se for Se-rich conditions.
- Under Sb-rich conditions, the crystal domain is small and grains grow in a disordered manner. In Se-rich films, grains are as thick as the layer itself with only grain boundaries parallel to device thickness.
- The crystalline orientation and structure of Sb_2Se_3 films are affected by the nominal Se content. A clear tendency toward an improved (002) orientation is maintained until stoichiometry is reached (most likely related to the

https://doi.org/10.1021/acsami.1c20764
ACS Appl. Mater. Interfaces 2022, 14, 11222−11234

increased annealing times and fewer impurity phases when approaching the 0.50 threshold). In contrast, for the increased Se content, the presence of $MoSe_2$ in the rear contact of the films plays a crucial role in the growth of well-oriented polycrystalline layers, leading to an abrupt enhancement of the (002) reflections.

Absorption Coefficient. Finally, photothermal deflection spectroscopy (PDS) was used to study the effect of varying the overall Se amount on the optical band gap and Urbach energy of Glass/Sb_2Se_3 samples. This information is very relevant since it allows us to assess the degree up to which changes in the nominal composition can affect intrinsic properties of the material, such as band gap energy. Also, exponentially decaying density of state (DOS) tails due to low-quality crystalline materials may cause transitions between these energy states inside the band gap (Urbach tails), which are characterized by the Urbach energy (U_0), leading to sub-band gap absorption. It is known that U_0 has an impact on carrier mobility and lifetime, affecting the device performance, especially the open-circuit voltage.[60,61] Hence, by computing U_0, it is possible to characterize the influence of modifying the overall Se content on the performance of the cell, with regard to the presence of band tails. Also, considering that these observations relate only to the absorber rather than the complete junction, they allow us to decorrelate the limitations from the films and the limitations from a specific junction, such as interfacial intermixing and band alignment, offering a good approach to characterize the defects of the material itself.

The absorption coefficient α is represented as a function of the energy of the incident (exciting) beam in Figure 5a. It is

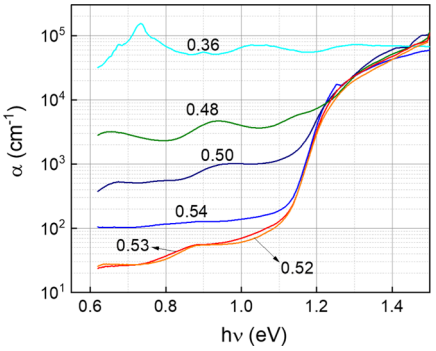

Figure 5. Absorption coefficient (α) as a function of photon energy ($h\nu$) of glass/Sb_2Se_3 films prepared during the same synthesis process as the SLG/Mo/Sb_2Se_3 corresponding samples with 2[Se]/(2[Se] + 3[Sb]): 0.54, 0.53, 0.50, 0.48, and 0.36. The absorption coefficient obtained from the PDS spectra.

clear that the sub-band gap absorption increases very significantly as the overall Se amount decreases. For instance, the sample with 0.36 Se (2[Se]/(2[Se] + 3[Sb])) does not even show a band gap decay, which could result from the large number of secondary phases (see XPS results, Figure 2), masking the Sb_2Se_3 absorption and leading to a very high α below the Sb_2Se_3 band gap (in the order of 10^5 cm^{-1}). Otherwise, improvements when switching from the stoichiometry (0.50) toward Se-rich conditions (0.52, 0.53) are noticed—the absorption coefficient inside the band gap decreases from 10^3 to 10^1 cm^{-1} (2 orders of magnitude). In the absence of a more detailed study on the effects of intrinsic doping for a very small interval around the stoichiometry, this significant decrease in the sub-band gap absorption may be due to compensation of deep defects. Interestingly, the samples with the lowest subgap α are those with 0.52 and 0.53 Se, whereas those with 0.54 are slightly higher, suggesting that a large Se excess can be detrimental to the absorber, possibly due to the appearance of Se secondary phases on the surface (see Raman spectra with elemental Se peaks in Figure S6). The effect of Se phases in the front interface could be assessed by comparing as-grown samples with films subjected to selective or complete surface etching (Br_2).[62−64] Other than that, the larger subgap absorption in Se-richer thin films could also be due to the recently reported abnormal defect behavior in Sb_2Se_3, which causes the density of Se vacancies V_{Se} to increase as the material becomes anion-richer, leading to general deteriorated performance in extremely Se-rich films.[65]

Tauc plots were computed from the PDS-derived α, from which the value of the optical band gap was extrapolated; see the obtained values in Table 1. Note that all values are

Table 1. Optical Band Gap (eV) and Urbach Energy (meV) in Relation to the Nominal Se Content in the Samples

Se content	band gap (eV)	Urbach energy (meV)
0.48	1.153 ± 0.022	70.12 ± 0.91
0.50	1.150 ± 0.027	41.80 ± 1.20
0.52	1.144 ± 0.012	24.80 ± 0.37
0.53	1.151 ± 0.008	23.49 ± 0.34
0.54	1.154 ± 0.006	22.99 ± 0.32

comparable considering the uncertainty. This confirms our hypothesis that Sb_2Se_3 is a stoichiometric material. Even though different nominal compositions have been explored, the band gap remains unchanged, indicating that no compositional changes of the Sb_2Se_3 phase are expected. Finally, the Urbach energy is determined in accordance with eq 3, where α_0 and U_1 are constants determined by fits to the experiment, h is Planck's constant, and ν is the incident beam frequency. Therefore, U_0 is obtained from the inverse of the slope resulting from plotting $\ln(\alpha)$ as a function of energy; see results in Table 1.[17] In the Se-rich range, U_0 is low (23−24 meV), indicating a good-quality absorber with a small number of absorption centers inside the band gap. Significantly, the Urbach energy in the Se-rich range is lower than other reported U_0 values from Sb_2Se_3-evaporated films.[17,66] Nonetheless, values shown here are still above the 20 meV barrier, which has been indicated to be one of the factors contributing to the large V_{oc} deficit in CIGS and CZTSSe technologies.[60] On the other hand, when the overall Se amount decreases, the Urbach energy increases steadily. As stated above, all previous measurements point toward a stoichiometric Sb_2Se_3 layer regardless of the synthesis conditions. Hence, variations in U_0 are likely due to increased disorder of the material, resulting from nonoptimal growth conditions, such as the presence of Sb_2O_3 and Sb preventing good crystalline growth (small, randomly oriented grains under Sb-rich conditions; see Figure 2). Changes in Urbach energy can also be connected to modifications in the defect structure of the material, where deep defects are compensated under Se-rich conditions but are prominent under Sb-rich conditions, all included inside the Sb_2Se_3 doping level. Considering both the very low sub-band gap absorption and U_0 of Se-rich Sb_2Se_3 thin films, it is expected that these can lead to better performing devices.

https://doi.org/10.1021/acsami.1c20764
ACS Appl. Mater. Interfaces 2022, 14, 11222−11234

$$\alpha = \alpha_0 \cdot \exp[\frac{h\upsilon - U_1}{U_0}] \quad (3)$$

Discussion of Structural and Optical Characterization and Its Translation to the Optoelectronic Properties of Devices. With the results of the compositional analysis presented above, a phase diagram has been developed; see Figure 6. Accordingly, note that the XRD analysis (Figure 6a)

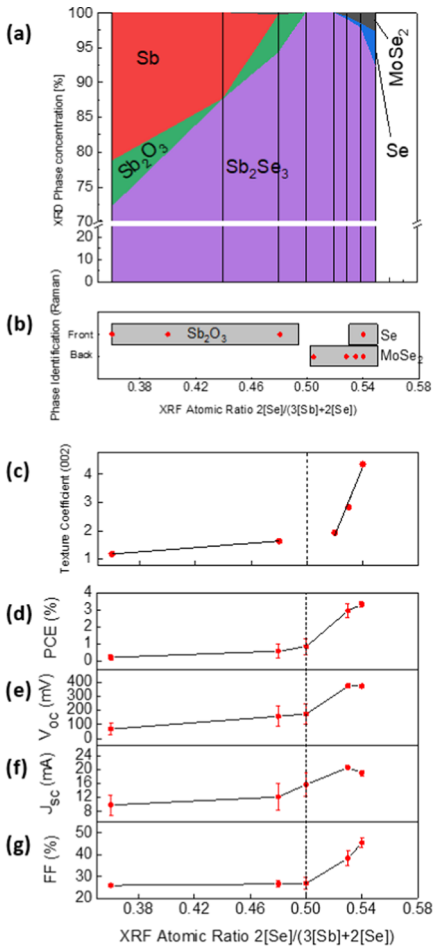

Figure 6. (a) Phase concentration extracted from XRD as a function of 2[Se]/(2[Se] + 3[Sb]). (b) Phases identified by Raman spectroscopy analysis as a function of 2[Se]/(2[Se] + 3[Sb]). (c) Texture coefficient (002) as a function of 2[Se]/(2[Se] + 3[Sb]). (d–g) Evolution of the optoelectronic parameters as a function of 2[Se]/(2[Se] + 3[Sb]).

shows different secondary phases depending on whether the material is under Se-rich or Sb-rich conditions, suggesting that Sb_2Se_3 does not allow an extended off-stoichiometry range. Instead, Sb excesses are either converted into Sb_2O_3 or remain as unreacted m-Sb, whereas Se excesses diffuse toward the Mo back contact, forming a $MoSe_2$ layer. Nevertheless, XRD tends to underestimate the $MoSe_2$ content, which has been detected in all Se-rich films analyzed by Raman spectroscopy (Figure 6b), demonstrating that $MoSe_2$ appears systematically in the Mo/absorber interface of Se-rich Sb_2Se_3. Therefore, combining XRD and Raman, it can be inferred that Sb_2Se_3 is a stoichiometric material, highly resilient to compositional changes, with any Sb or Se excesses compensated in the form of metallic Sb, Sb_2O_3 (Sb-rich), or $MoSe_2$ (Se-rich). Moving further away from the stoichiometry toward Sb-rich conditions, the amount of unreacted Sb increases. On the other hand, for 2[Se]/(2[Se] + 3[Sb]) > 0.54, Se elemental phases appear, which could likely be a limitation for electronic transport.

So far, the effect of varying the overall Se concentration in Sb_2Se_3 on the intrinsic properties of the absorber (structure, composition, morphology) has been considered, regardless of how it might affect its PV performance. To investigate the optoelectronic properties of nonstoichiometric Sb_2Se_3-based solar cells, $J-V$ curves of a selected set of samples have been acquired, which are processed into PV devices with the following architecture: Mo/Sb_2Se_3/CdS/ZnO/ITO. The results from this study are shown in Figure 6d–g, where the power conversion efficiency (PCE), V_{oc}, J_{sc}, and fill factor (FF) have been plotted as a function of 2[Se]/(2[Se] + 3[Sb]). Notice that PCE and V_{oc} follow similar trends (Figure 6d,e), with the devices prepared from absorbers with 0.36 and 0.48 Se showing the lowest V_{oc} (66 and 157 mV, respectively), which could be due to the abundant secondary phases appearing under Sb-rich conditions, the high Urbach energy (see Table 1), and the extremely large sub-band gap absorption (see PDS results in Figure 5a). These secondary phases include an Sb_2O_3 layer in front of the cell (see XPS profiles in Figure 1), thicker than a few nanometers, and possibly inhomogeneous morphology is likely to disrupt the Sb_2Se_3/CdS interface, preventing a good performance of the p-n junction. On the other hand, both 0.53 and 0.54 Se films exhibit a good PCE and V_{oc} of around 4% and 400 mV, respectively, with which it is shown that a small deviation toward Se-poor compositions is much more detrimental to the operation of the device than switching toward Se-rich conditions. However, as the Se amount continues to increase, a small reduction in J_{sc} is observed (see Figure 6f), which could result from the appearance of Se elemental phases at the heterointerface with CdS (Figure S6).

More interestingly, the sample with 0.50 Se (strictly stoichiometric) shows low PCE, V_{oc}, and FF, when under these conditions of absence of impurity phases, much higher values, or at least similar to those of the 0.53 and 0.54 films (Se-rich), would be expected. On the one hand, the better performance of Se-rich films could be due to the compensation of V_{Se} defects, which might act as effective recombination centers.[26] On the other hand, the reported declining trends in V_{oc} and FF coincide with the loss of a (002)-preferred crystalline orientation when the Se content decreases, as shown by TC_{002} in Figure 6c. Indeed, all optoelectronic parameters in the range of 0.36 < 2[Se]/(2[Se] + 3[Sb]) < 0.54 present the characteristic double-slope trend of TC_{002}, indicating a strong dependence of Sb_2Se_3 PV performance on the crystalline orientation. A deterioration in the ribbon alignment implies the loss of the enhanced c-axis conductivity due to the anisotropic properties of Sb_2Se_3, causing a sharp drop in the PV performance.

Furthermore, it is observed that while the $MoSe_2$ content gradually decreases until it stops forming for Sb-rich samples, TC_{002} decreases steeply to values between 1 and 2. Afterward, the (002)-preferred orientation continues dwindling, but with a much lower rate. Therefore, it is likely that the existence of a $MoSe_2$ phase plays a relevant role in the well-oriented growth of quasi-1D Sb_2Se_3. Thus, a certain amount and good crystalline orientation of $MoSe_2$ can decisively influence the preferential orientation of Sb_2Se_3, improving its optoelectronic

https://doi.org/10.1021/acsami.1c20764
ACS Appl. Mater. Interfaces 2022, 14, 11222–11234

properties. Certainly, by the XRD−Rietveld analysis, it has been noticed that the $MoSe_2$ has a preferred crystalline orientation in the (001) direction, confirming its role in enhancing the Sb_2Se_3 grain growth perpendicular to the substrate (see Table S1).

Overall, these results clearly point out in the direction that Sb_2Se_3 is a single-phase material that does not admit significant off-stoichiometric variations, whose crystalline orientation is essential to develop good PV performance, and for which the growing conditions, in particular with regard to the formation of certain phases, can either improve or deteriorate its structural and electronic properties. However, the study presented here has some limitations. For instance, although it confirms previously reported improvements of incorporating a $MoSe_2$ layer in Mo/Sb_2Se_3 devices[48] (in this case by *in situ* formation of $MoSe_2$ during the Sb_2Se_3 reactive annealing), no specific analysis of the $MoSe_2$ phase has been performed. Thus, we believe that studying the formation process and properties of the $MoSe_2$ phase in detail could help to clear up some of the hypotheses raised in this work, such as the specific effect it exerts on the Sb_2Se_3 crystalline growth. Furthermore, results suggest that the Sb_2Se_3 formation by reactive annealing constitutes a dynamic process, in which there is a Se flux through the Sb layer, and then, the absorber crystallizes upon reaching 320 °C, validating the premise that the back contact's texture has an impact on the Sb_2Se_3 structure. However, the precise formation mechanism should be investigated further—we suggest performing complete characterization analysis of samples acquired by interrupted growth at different annealing times.[41] Also, this work is essentially centered on the standard process for preparing Sb_2Se_3 thin films in the substrate configuration (i.e., Mo/Sb_2Se_3/buffer layer/TCO), leading to the formation of the $MoSe_2$ layer under Se-excess conditions. Notwithstanding, we believe that it might be interesting to investigate what happens when there is no Mo resource available. Under these circumstances, it may be possible that the Se surplus is effectively incorporated into the Sb_2Se_3 structure or else it accumulates at the front interface in the form of elemental Se, as has been suggested elsewhere.[67−69] Further research and supporting evidence for verification are required.

In this work, we have shown that there is a direct correlation between Raman spectra and (002) crystalline orientation, which so far has been justified based on a comparative study of Raman analysis and XRD (especially TC calculations); however, additional support is required, for example, by studying the Raman spectra of Sb_2Se_3 grown on different substrates or using synthetic routes that give rise to different textures. Otherwise, further study of Sb_2Se_3 in the Se-rich range might be necessary to unequivocally identify the nature of the elemental Se phases that appear under these conditions and hence design strategies to remove or minimize them, such as etching procedures. Finally, we emphasize that this study has been based on investigating the consequences of significantly modifying the nominal concentration of Sb_2Se_3 films; however, focusing on a very small interval around the stoichiometry might shed new light on the effect of intrinsic doping, especially with regard to reducing the amount of V_{Se} defects.

CONCLUSIONS

In this work, it has been confirmed that Mo/Sb_2Se_3 thin films do not allow an extended off-stoichiometry range, whereby any Sb or Se excess is compensated in the form of secondary phases: $MoSe_2$ and Se elemental phases under Se-rich compositional conditions and Sb_2O_3 and m-Sb in the Sb-rich range. The results presented here illustrate the difficulty of selectively controlling or enhancing the formation of Sb_2Se_3 intrinsic properties (e.g, defects) by modulating the Se chemical potential beyond stoichiometric conditions, unlike CIGS or CZTS. Hence, we suggest that enhancing the many virtues of Sb_2Se_3 (and minimizing its numerous defects) will require exploring new opportunities through extrinsic doping or alloying. For instance, the similar behavior of Sb_2Se_3 to that of CdTe makes us think about the suitability of applying successful recipes in CdTe to unlock the full potential of Sb_2Se_3. Second, it has been shown that despite the fact that Sb_2Se_3 is stoichiometric, it is necessary to operate under Se-rich conditions to develop good devices, primarily to form a $MoSe_2$ phase — promoting a well-oriented growth in the (002)-crystalline direction and avoiding the appearance of unwanted secondary phases — and also to minimize the number of detrimental V_{Se}-type defects, although this aspect needs to be investigated further. We demonstrate that $MoSe_2$ plays a dual role, as a hole transport layer and as a growth matrix, directing and effectively influencing the structural characteristics of Sb_2Se_3.[70] Ultimately, this study has shown the power of Raman−XRD-related combined techniques to examine the structural properties of Sb_2Se_3, especially the degree of orientation in the (001) direction, and PDS to obtain the sub-band gap absorption and U_0, which need to be minimized to develop good absorbers. Overall, this work points out at new strategies to improve Sb_2Se_3 devices, including extrinsic doping approaches rather than intrinsic doping (due to the small gap free of damaging secondary phases when the composition shifts away from stoichiometry) and etching treatments for Se-rich samples (to take advantage of the $MoSe_2$ formation, while eliminating the surface elemental Se disruptive phases).

ASSOCIATED CONTENT

Supporting Information

The Supporting Information is available free of charge at https://pubs.acs.org/doi/10.1021/acsami.1c20764.

Description of the procedure to obtain the absorption coefficient by PDS; additional XPS, XRD Raman, and SEM figures; and XRD analysis and Rietveld parameters (PDF)

AUTHOR INFORMATION

Corresponding Author

Ivan Caño − *Escola d'Enginyeria de Barcelona Est (EEBE), Universitat Politècnica de Catalunya, 08019 Barcelona, Spain*; orcid.org/0000-0003-4226-1527; Email: ivan.cano.prades@upc.edu

Authors

Pedro Vidal-Fuentes − *Institut de Recerca en Energia de Catalunya (IREC), 08930 Sant Adrià del Besòs, Spain*; orcid.org/0000-0001-5776-9986

Lorenzo Calvo-Barrio − *Centres Científics i Tecnològics (CCiTUB), Universitat de Barcelona, 08028 Barcelona, Spain; IN2UB, Departament d'Enginyeria Electrònica i Biomèdica, Universitat de Barcelona, 08028 Barcelona, Spain*

Xavier Alcobé − *Centres Científics i Tecnològics (CCiTUB), Universitat de Barcelona, 08028 Barcelona, Spain*

https://doi.org/10.1021/acsami.1c20764
ACS Appl. Mater. Interfaces 2022, 14, 11222−11234

José Miguel Asensi − *Departament de Física Aplicada, Universitat de Barcelona, 08028 Barcelona, Spain*
Sergio Giraldo − *Institut de Recerca en Energia de Catalunya (IREC), 08930 Sant Adrià del Besòs, Spain;* orcid.org/0000-0003-4881-5041
Yudania Sánchez − *Institut de Recerca en Energia de Catalunya (IREC), 08930 Sant Adrià del Besòs, Spain;* orcid.org/0000-0002-5740-1150
Zacharie Jehl − *Escola d'Enginyeria de Barcelona Est (EEBE), Universitat Politècnica de Catalunya, 08019 Barcelona, Spain;* orcid.org/0000-0002-2610-5973
Marcel Placidi − *Escola d'Enginyeria de Barcelona Est (EEBE), Universitat Politècnica de Catalunya, 08019 Barcelona, Spain;* orcid.org/0000-0001-5684-9669
Joaquim Puigdollers − *Escola d'Enginyeria de Barcelona Est (EEBE), Universitat Politècnica de Catalunya, 08019 Barcelona, Spain;* orcid.org/0000-0002-1834-2565
Victor Izquierdo-Roca − *Institut de Recerca en Energia de Catalunya (IREC), 08930 Sant Adrià del Besòs, Spain*
Edgardo Saucedo − *Escola d'Enginyeria de Barcelona Est (EEBE), Universitat Politècnica de Catalunya, 08019 Barcelona, Spain*

Complete contact information is available at: https://pubs.acs.org/10.1021/acsami.1c20764

Author Contributions

I.C. performed the synthesis procedure of samples, analyzed results from XRD, Raman, and PDS techniques, and wrote the article. P.V. performed the PDS measurements and data analysis and contributed to the writing of the article. L.C. conducted the XPS measurements and data analysis. X.A. performed the XRD measurements and Rietveld analysis. J.A. contributed to the article by providing PDS equipment and measurements. S.G. conducted the SEM measurements. Y.S. participated in the synthesis of PV devices (chemical treatments). Z.J., M.P., and E.S. contributed to the conceptualization of research and to the writing of the article (review and editing). J.P, V.I., and E.S. contributed to the conceptualization of research and provided funding and resources. All authors have given approval to the final version of the manuscript.

Notes

The authors declare no competing financial interest.

■ ACKNOWLEDGMENTS

This research has received funding from the European Union H2020 Framework Programme under Grant Agreement no. 866018, Low dimensional semiconductors for optically tuneable solar harvesters (SENSATE), by the Spanish Ministry of Science, Innovation and Universities under the MATER-ONE project (PID2020-116719RB-C41), and by the European Regional Development Funds (ERDF, FEDER Programa Competitivitat de Catalunya 2007−2013). The authors from the IREC and the University of Barcelona belong to the SEMS (Solar Energy Materials and Systems) Consolidated Research Group of the "Generalitat de Catalunya" (ref 2017 SGR 862). M.P. acknowledges the financial support from Spanish Ministry of Science, Innovation and Universities within the Ramon y Cajal program (IJC2018-038199-I).

■ REFERENCES

(1) Green, M. A.; Hishikawa, Y.; Warta, W.; Dunlop, E. D.; Levi, D. H.; Hohl-Ebinger, J.; Ho-Baillie, A. W. H. Solar Cell Efficiency Tables (Version 50). *Prog. Photovoltaics* **2017**, *25*, 668−676.
(2) Nakamura, M.; Yamaguchi, K.; Kimoto, Y.; Yasaki, Y.; Kato, T.; Sugimoto, H. Cd-Free Cu(In,Ga)(Se,S)2 Thin-Film Solar Cell with Record Efficiency of 23.35%. *IEEE J. Photovoltaics* **2019**, *9*, 1863−1867.
(3) Watari, T.; Nansai, K.; Nakajima, K. Review of Critical Metal Dynamics to 2050 for 48 Elements. *Resour., Conserv. Recycl.* **2020**, *155*, No. 104669.
(4) Candelise, C.; Winsker, M.; Gross, R. Implications for CdTr and CIGS Technologies Production Costs of Indium and Tellurium Scarcity. *Prog. Photovoltaics* **2012**, *20*, 1114−1129.
(5) Fthenakis, V. Sustainability of Photovoltaics: The Case for Thin-Film Solar Cells. *Renewable Sustainable Energy Rev.* **2009**, *13*, 2746−2750.
(6) Wong, L. H.; Zakutayev, A.; Major, J. D.; Hao, X.; Walsh, A.; Todorov, T. K.; Saucedo, E. Emerging Inorganic Solar Cell Efficiency Tables (Version 1). *J. Phys.: Energy* **2019**, *1*, No. 032001.
(7) Kim, S.; Márquez, J. A.; Unold, T.; Walsh, A. Upper Limit to the Photovoltaic Efficiency of Imperfect Crystals from First Principles. *Energy Environ. Sci.* **2020**, *13*, 1481−1491.
(8) Schorr, S.; Gurieva, G.; Guc, M.; Dimitrievska, M.; Pérez-Rodríguez, A.; Izquierdo-Roca, V.; Schnohr, C. S.; Kim, J.; Jo, W.; Merino, J. M. Point Defects, Compositional Fluctuations, and Secondary Phases in Non-Stoichiometric Kesterites. *J. Phys. Energy* **2020**, *2*, No. 012002.
(9) Giraldo, S.; Jehl, Z.; Placidi, M.; Izquierdo-Roca, V.; Pérez-Rodríguez, A.; Saucedo, E. Progress and Perspectives of Thin Film Kesterite Photovoltaic Technology: A Critical Review. *Adv. Mater.* **2019**, *31*, No. 1806692.
(10) Chen, C.; Li, W.; Zhou, Y.; Chen, C.; Luo, M.; Liu, X.; Zeng, K.; Yang, B.; Zhang, C.; Han, J.; Tang, J. Optical Properties of Amorphous and Polycrystalline Sb2Se3 Thin Films Prepared by Thermal Evaporation. *Appl. Phys. Lett.* **2015**, *107*, No. 043905.
(11) Li, Z.; Liang, X.; Li, G.; Liu, H.; Zhang, H.; Guo, J.; Chen, J.; Shen, K.; San, X.; Yu, W.; Schropp, R. E. I.; Mai, Y. 9.2%-Efficient Core-Shell Structured Antimony Selenide Nanorod Array Solar Cells. *Nat. Commun.* **2019**, *10*, No. 125.
(12) Shen, K.; Zhang, Y.; Wang, X.; Ou, C.; Guo, F.; Zhu, H.; Liu, C.; Gao, Y.; Schropp, R. E. I.; Li, Z.; Liu, X.; Mai, Y. Efficient and Stable Planar n−i−p Sb2Se3 Solar Cells Enabled by Oriented 1D Trigonal Selenium Structures. *Adv. Sci.* **2020**, *7*, No. 2001013.
(13) Mavlonov, A.; Razykov, T.; Raziq, F.; Gan, J.; Chantana, J.; Kawano, Y.; Nishimura, T.; Wei, H.; Zakutayev, A.; Minemoto, T.; Zu, X.; Li, S.; Qiao, L. A Review of Sb2Se3 Photovoltaic Absorber Materials and Thin-Film Solar Cells. *Sol. Energy* **2020**, *201*, 227−246.
(14) Yang, L.; Hong, W.; Tian, Y.; Zou, G.; Hou, H.; Sun, W.; Ji, X. Heteroatom-Doped Carbon Inlaid with Sb2X3 (X = S, Se) Nanodots for High-Performance Potassium-Ion Batteries. *Chem. Eng. J.* **2020**, *385*, No. 123838.
(15) Wang, J.; Liu, Z.; Zhou, J.; Han, K.; Lu, B. Insights into Metal/Metalloid-Based Alloying Anodes for Potassium Ion Batteries. *ACS Mater. Lett.* **2021**, *3*, 1572−1598.
(16) Zhou, Y.; Wang, L.; Chen, S.; Qin, S.; Liu, X.; Chen, J.; Xue, D. J.; Luo, M.; Cao, Y.; Cheng, Y.; Sargent, E. H.; Tang, J. Thin-Film Sb2Se3 Photovoltaics with Oriented One-Dimensional Ribbons and Benign Grain Boundaries. *Nat. Photonics* **2015**, *9*, 409−415.
(17) Chen, C.; Bobela, D. C.; Yang, Y.; Lu, S.; Zeng, K.; Ge, C.; Yang, B.; Gao, L.; Zhao, Y.; Beard, M. C.; Tang, J. Characterization of Basic Physical Properties of Sb2Se3 and Its Relevance for Photovoltaics. *Front. Optoelectron.* **2017**, *10*, 18−30.
(18) Zhou, J.; Chen, H.; Zhang, X.; Chi, K.; Cai, Y.; Cao, Y.; Âng, J. Substrate Dependence on (Sb4Se6)n Ribbon Orientations of Antimony Selenide Thin Films: Morphology, Carrier Transport and Photovoltaic Performance. *J. Alloys Compd.* **2021**, *862*, No. 158703.
(19) Pattini, F.; Rampino, S.; Mezzadri, F.; Calestani, D.; Spaggiari, G.; Sidoli, M.; Delmonte, D.; Sala, A.; Gilioli, E.; Mazzer, M. Role of

the Substrates in the Ribbon Orientation of Sb2Se3 Films Grown by Low-Temperature Pulsed Electron Deposition. *Sol. Energy Mater. Sol. Cells* **2020**, *218*, No. 110724.
(20) Park, S. N.; Kim, S. Y.; Lee, S. J.; Sung, S. J.; Yang, K. J.; Kang, J. K.; Kim, D. H. Controlled Synthesis of (:Hk 1) Preferentially Oriented Sb2Se3 Rod Arrays by Co-Evaporation for Photovoltaic Applications. *J. Mater. Chem. A* **2019**, *7*, 25900−25907.
(21) Rijal, S.; Li, D.; Awni, R. A.; Xiao, C.; Bista, S. S.; Jamarkattel, M. K.; Heben, M. J.; Jiang, C.; Al-Jassim, M.; Song, Z.; Yan, Y. Templated Growth and Passivation of Vertically Oriented Antimony Selenide Thin Films for High-Efficiency Solar Cells in Substrate Configuration. *Adv. Funct. Mater.* **2021**, No. 2110032.
(22) Liang, G. X.; Luo, Y.; di Chen, S.; Tang, R.; Zheng, Z. H.; Li, X. J.; Liu, X. S.; Liu, Y. K.; Li, Y. F.; Chen, X. Y.; Su, Z. H.; Zhang, X. H.; Ma, H. L.; Fan, P. Sputtered and Selenized Sb2Se3 Thin-Film Solar Cells with Open-Circuit Voltage Exceeding 500 MV. *Nano Energy* **2020**, *73*, No. 104806.
(23) Fan, P.; Chen, G. J.; Chen, S.; Zheng, Z. H.; Azam, M.; Ahmad, N.; Su, Z. H.; Liang, G. X.; Zhang, X. H.; Chen, Z. G. Quasi-Vertically Oriented Sb2Se3Thin-Film Solar Cells with Open-Circuit Voltage Exceeding 500 MV Prepared via Close-Space Sublimation and Selenization. *ACS Appl. Mater. Interfaces* **2021**, *13*, 46671−46680.
(24) Savory, C. N.; Scanlon, D. O. The Complex Defect Chemistry of Antimony Selenide. *J. Mater. Chem. A* **2019**, *7*, 10739−10744.
(25) Mavlonov, A.; Razykov, T.; Raziq, F.; Gan, J.; Chantana, J.; Kawano, Y.; Nishimura, T.; Wei, H.; Zakutayev, A.; Minemoto, T.; Zu, X.; Li, S.; Qiao, L. A Review of Sb2Se3 Photovoltaic Absorber Materials and Thin-Film Solar Cells. *Sol. Energy* **2020**, *201*, 227−246.
(26) Huang, M.; Xu, P.; Han, D.; Tang, J.; Chen, S. Complicated and Unconventional Defect Properties of the Quasi-One-Dimensional Photovoltaic Semiconductor Sb2Se3. *ACS Appl. Mater. Interfaces* **2019**, *11*, 15564−15572.
(27) Turcu, M.; Pakma, O.; Rau, U. Interdependence of Absorber Composition and Recombination Mechanism in Cu(In, Ga)(Se, S)2 Heterojunction Solar Cells. *Appl. Phys. Lett.* **2002**, *80*, 2598−2600.
(28) Siebentritt, S.; Gütay, L.; Regesch, D.; Aida, Y.; Deprédurand, V. Why Do We Make Cu(In,Ga)Se2 Solar Cells Non-Stoichiometric? *Sol. Energy Mater. Sol. Cells* **2013**, *119*, 18−25.
(29) Herberholz, R.; Nadenau, V.; Rühle, U.; Köble, C.; Schock, H. W.; Dimmler, B. Prospects of Wide-Gap Chalcopyrites for Thin Film Photovoltaic Modules. *Sol. Energy Mater. Sol. Cells* **1997**, *49*, 227−237.
(30) Chen, S.; Walsh, A.; Gong, X. G.; Wei, S. H. Classification of Lattice Defects in the Kesterite Cu2ZnSnS 4 and Cu2ZnSnSe4 Earth-Abundant Solar Cell Absorbers. *Adv. Mater.* **2013**, *25*, 1522−1539.
(31) Romanyuk, Y. E.; Haass, S. G.; Giraldo, S.; Placidi, M.; Tiwari, D.; Fermin, D. J.; Hao, X.; Xin, H.; Schnabel, T.; Kauk-Kuusik, M.; Pistor, P.; Lie, S.; Wong, L. H. Doping and Alloying of Kesterites. *J. Phys.: Energy* **2019**, *1*, No. 044004.
(32) Vidal-Fuentes, P.; Placidi, M.; Sánchez, Y.; Becerril-Romero, I.; Andrade-Arvizu, J.; Jehl, Z.; Pérez-Rodríguez, A.; Izquierdo-Roca, V.; Saucedo, E. Efficient Se-Rich Sb2Se3/CdS Planar Heterojunction Solar Cells by Sequential Processing: Control and Influence of Se Content. *Sol. RRL* **2020**, *4*, No. 2000141.
(33) Liu, X.; Qiao, Y.; Liu, Y.; Liu, J.; Jia, E.; Chang, S.; Shen, X.; Li, S.; Cheng, K. Enhanced Open Circuit Voltage of Sb2Se3/CdS Solar Cells by Annealing Se-Rich Amorphous Sb2Se3 Films Prepared via Sputtering Process. *Sol. Energy* **2020**, *195*, 697−702.
(34) Courel, M.; Valencia-Resendiz, E.; Andrade-Arvizu, J. A.; Saucedo, E.; Vigil-Galán, O. Towards Understanding Poor Performances in Spray-Deposited Cu2ZnSnS4thin Film Solar Cells. *Sol. Energy Mater. Sol. Cells* **2017**, *159*, 151−158.
(35) Rietveld, H. M. A Profile Refinement Method for Nuclear and Magnetic Structures. *J. Appl. Crystallogr.* **1969**, *2*, 65−71.
(36) Coelho, A. A.; Evans, J.; Evans, I.; Kern, A.; Parsons, S. The T OPAS Symbolic Computation System. *Powder Diffr.* **2011**, *26*, S22−S25.
(37) Balzar, D.; Audebrand, N.; Daymond, M. R.; Fitch, A.; Hewat, A.; Langford, J. I.; le Bail, A.; Louër, D.; Masson, O.; McCowan, C. N.; Popa, N. C.; Stephens, P. W.; Toby, B. H. Size-Strain Line-Broadening Analysis of the Ceria Round-Robin Sample. *J. Appl. Crystallogr.* **2004**, *37*, 911−924.
(38) Whitfield, P. S. Spherical Harmonics Preferential Orientation Corrections and Structure Solution from Powder Diffraction Data—A Possible Avenue of Last Resort. *J. Appl. Crystallogr.* **2009**, *42*, 134−136.
(39) Cheary, R. W.; Coelho, A. A.; Cline, J. P. Fundamental Parameters Line Profile Fitting in Laboratory Diffractometers. *J. Res. Natl. Inst. Stand. Technol.* **2007**, *109*, 1−25.
(40) Serra, J.; Andreu, J.; Sardin, G.; Roch, C.; Asensi, J. M.; Bertomeu, J.; Esteve, J. Hydrogen Related Effects in A-Si:H Studied by Photothermal Deflection Spectroscopy. *Phys. B* **1991**, *170*, 269−272.
(41) Giraldo, S.; Saucedo, E.; Neuschitzer, M.; Oliva, F.; Placidi, M.; Alcobé, X.; Izquierdo-Roca, V.; Kim, S.; Tampo, H.; Shibata, H.; Pérez-Rodríguez, A.; Pistor, P. How Small Amounts of Ge Modify the Formation Pathways and Crystallization of Kesterites. *Energy Environ. Sci.* **2018**, *11*, 582−593.
(42) Lopez-Marino, S.; Espíndola-Rodríguez, M.; Sánchez, Y.; Alcobé, X.; Oliva, F.; Xie, H.; Neuschitzer, M.; Giraldo, S.; Placidi, M.; Caballero, R.; Izquierdo-Roca, V.; Pérez-Rodríguez, A.; Saucedo, E. The Importance of Back Contact Modification in Cu2ZnSnSe4 Solar Cells: The Role of a Thin MoO2 Layer. *Nano Energy* **2016**, *26*, 708−721.
(43) Shin, B.; Zhu, Y.; Bojarczuk, N. A.; Jay Chey, S.; Guha, S. Control of an Interfacial MoSe 2 Layer in Cu 2ZnSnSe 4 Thin Film Solar Cells: 8.9 Power Conversion Efficiency with a TiN Diffusion Barrier. *Appl. Phys. Lett.* **2012**, *101*, No. 053903.
(44) Wada, T.; Kohara, N.; Nishiwaki, S.; Negami, T. Characterization of the Cu(In,Ga)Se2/Mo Interface in CIGS Solar Cells. *Thin Solid Films* **2001**, *387*, 118−122.
(45) Balasingam, S. K.; Lee, J. S.; Jun, Y. Few-Layered MoSe2 Nanosheets as an Advanced Electrode Material for Supercapacitors. *Dalton Trans.* **2015**, *44*, 15491−15498.
(46) Nishiwaki, S.; Kohara, N.; Negami, T.; Wada, T. MoSe2 Layer Formation at Cu (In, Ga) Se 2 / Mo Interfaces in High Efficiency Cu $(In_{1-x}Ga_x)$ Se2 Solar Cells. *Jpn. J. Appl. Phys* **1998**, *37*, L71−L73.
(47) Lee, D.; Cho, J. Y.; Heo, J. Improved Efficiency of Sb2Se3/CdS Thin-Film Solar Cells: The Effect of Low-Temperature Pre-Annealing of the Absorbers. *Sol. Energy* **2018**, *173*, 1073−1079.
(48) Li, Z.; Chen, X.; Zhu, H.; Chen, J.; Guo, Y.; Zhang, C.; Zhang, W.; Niu, X.; Mai, Y. Sb2Se3 Thin Film Solar Cells in Substrate Configuration and the Back Contact Selenization. *Sol. Energy Mater. Sol. Cells* **2017**, *161*, 190−196.
(49) Vidal-Fuentes, P.; Guc, M.; Alcobe, X.; Jawhari, T.; Placidi, M.; Pérez-Rodríguez, A.; Saucedo, E.; Roca, V. I. Multiwavelength Excitation Raman Scattering Study of Sb2Se3 Compound: Fundamental Vibrational Properties and Secondary Phases Detection. *2D Mater.* **2019**, *6*, No. 045054.
(50) Shongalova, A.; Correia, M. R.; Vermang, B.; Cunha, J. M. V.; Salomé, P. M. P.; Fernandes, P. A. On the Identification of Sb2Se3 Using Raman Scattering. *MRS Commun.* **2018**, *8*, 865−870.
(51) Cody, C. A.; Dlcarlo, L.; Darlington, R. K. Vibrational and Thermal Study of Antimony Oxides. *Inorg. Chem.* **1979**, *18*, 1572−1576.
(52) Yannopoulos, S. N.; Andrikopoulos, K. S. Raman Scattering Study on Structural and Dynamical Features of Noncrystalline Selenium. *J. Chem. Phys.* **2004**, *121*, 4747−4758.
(53) Fleck, N.; Hobson, T. D. C.; Savory, C. N.; Buckeridge, J.; Veal, T. D.; Correia, M. R.; Scanlon, D. O.; Durose, K.; Jäckel, F. Identifying Raman Modes of Sb2Se3and Their Symmetries Using Angle-Resolved Polarised Raman Spectra. *J. Mater. Chem. A* **2020**, *8*, 8337−8344.
(54) Jin, X.; Fang, Y.; Salim, T.; Feng, M.; Yuan, Z.; Hadke, S.; Sum, T. C.; Wong, L. H. Controllable Solution-Phase Epitaxial Growth of Q1D Sb2(S,Se)3/CdS Heterojunction Solar Cell with 9.2% Efficiency. *Adv. Mater.* **2021**, *33*, No. 2104346.

(55) Olin, A.; Noläng, B.; Osadchi, E. G.; Öhman, L.-O.; Rosén, E. *Chemical Thermodynamics Of Selenium*; Elsevier, 2005.
(56) Cang, Q.; Guo, H.; Jia, X.; Ning, H.; Ma, C.; Zhang, J.; Yuan, N.; Ding, J. Enhancement in the Efficiency of Sb2Se3 Solar Cells by Adding Low Lattice Mismatch CuSbSe2 Hole Transport Layer. *Sol. Energy* **2020**, *199*, 19−25.
(57) Song, S. H.; Campbell, S. A. Heteroepitaxy and the Performance of CIGS Solar Cells. *Conf. Rec. IEEE Photovoltaic Spec. Conf.* **2013**, *2*, 2534−2539.
(58) Jain, S. C.; Harker, A. H.; Cowley, R. A. Misfit Strain and Misfit Dislocations in Lattice Mismatched Epitaxial Layers and Other Systems. *Philos. Mag. A* **1997**, *75*, 1461−1515.
(59) Bhattacharyya, A.; Maurice, D. On the Evolution of Stresses Due to Lattice Misfit at a Ni-Superalloy and YSZ Interface. *Surf. Interfaces* **2018**, *12*, 86−94.
(60) Chantana, J.; Kawano, Y.; Nishimura, T.; Mavlonov, A.; Minemoto, T. Impact of Urbach Energy on Open-Circuit Voltage Deficit of Thin-Film Solar Cells. *Sol. Energy Mater. Sol. Cells* **2020**, *210*, No. 110502.
(61) Choudhury, B.; Dey, M.; Choudhury, A. Defect Generation, d-d Transition, and Band Gap Reduction in Cu-Doped TiO2 Nanoparticles. *Int. Nano Lett.* **2013**, *3*, No. 25.
(62) Canava, B.; Guillemoles, J. F.; Vigneron, J.; Lincot, D.; Etcheberry, A. Chemical Elaboration of Well Defined Cu(In,Ga)Se2 Surfaces after Aqueous Oxidation Etching. *J. Phys. Chem. Solids* **2003**, *64*, 1791−1796.
(63) Bouttemy, M.; Tran-Van, P.; Gerard, I.; Hildebrandt, T.; Causier, A.; Pelouard, J. L.; Dagher, G.; Jehl, Z.; Naghavi, N.; Voorwinden, G.; Dimmler, B.; Powalla, M.; Guillemoles, J. F.; Lincot, D.; Etcheberry, A. Thinning of CIGS Solar Cells: Part I: Chemical Processing in Acidic Bromine Solutions. *Thin Solid Films* **2011**, *519*, 7207−7211.
(64) Jehl, Z.; Erfurth, F.; Naghavi, N.; Lombez, L.; Gerard, I.; Bouttemy, M.; Tran-Van, P.; Etcheberry, A.; Voorwinden, G.; Dimmler, B.; Wischmann, W.; Powalla, M.; Guillemoles, J. F.; Lincot, D. Thinning of CIGS Solar Cells: Part II: Cell Characterizations. *Thin Solid Films* **2011**, *519*, 7212−7215.
(65) Huang, M.; Cai, Z.; Wang, S.; Gong, X.; Wei, S.; Chen, S. More Se Vacancies in Sb 2 Se 3 under Se-Rich Conditions: An Abnormal Behavior Induced by Defect-Correlation in Compensated Compound Semiconductors. *Small* **2021**, *17*, No. 2102429.
(66) Ghosh, S.; Moreira, M. V. B.; Fantini, C.; González, J. C. Growth and Optical Properties of Nanocrystalline Sb2Se3 Thin-Films for the Application in Solar-Cells. *Solar Energy* **2020**, *211*, 613−621.
(67) Shongalova, A.; Correia, M. R.; Teixeira, J. P.; Leitão, J. P.; González, J. C.; Ranjbar, S.; Garud, S.; Vermang, B.; Cunha, J. M. V.; Salomé, P. M. P.; Fernandes, P. A. Growth of Sb2Se3 Thin Films by Selenization of RF Sputtered Binary Precursors. *Sol. Energy Mater. Sol. Cells* **2018**, *187*, 219−226.
(68) Wang, C.; Lu, S.; Li, S.; Wang, S.; Lin, X.; Zhang, J.; Kondrotas, R.; Li, K.; Chen, C.; Tang, J. Efficiency Improvement of Flexible Sb2Se3 Solar Cells with Non-Toxic Buffer Layer via Interface Engineering. *Nano Energy* **2020**, *71*, No. 104577.
(69) Kim, J.; Ji, S.; Jang, Y.; Jeong, G.; Choi, J.; Kim, D.; Nam, S. W.; Shin, B. Importance of Fine Control of Se Flux for Improving Performances of Sb2Se3 Solar Cells Prepared by Vapor Transport Deposition. *Solar RRL* **2021**, *5*, No. 2100327.
(70) Spies, J. A.; Schafer, R.; Wager, J. F.; Hersh, P.; Platt, H. A. S.; Keszler, D. A.; Schneider, G.; Kykyneshi, R.; Tate, J.; Liu, X.; Compaan, A. D.; Shafarman, W. N. Pin Double-Heterojunction Thin-Film Solar Cell P-Layer Assessment. *Sol. Energy Mater. Sol. Cells* **2009**, *93*, 1296−1308.

https://doi.org/10.1021/acsami.1c20764
ACS Appl. Mater. Interfaces 2022, 14, 11222−11234